A temperature-dependent critical Casimir patchy particle model benchmarked onto experiment

Jonas, H.J.; Stuij, S.G.; Schall, P.; Bolhuis, P.G.

DOI
10.1063/5.0055012

Publication date
2021

Document Version
Final published version

Published in
Journal of Chemical Physics

The Journal of Chemical Physics ARTICLE scitation.org/journal/jcp

A temperature-dependent critical Casimir patchy particle model benchmarked onto experiment

Cite as: J. Chem. Phys. 155, 034902 (2021); doi: 10.1063/5.0055012
Submitted: 24 April 2021 • Accepted: 23 June 2021 •
Published Online: 15 July 2021

H. J. Jonas,[1] S. G. Stuij,[2] P. Schall,[2] and P. G. Bolhuis[1,a)]

AFFILIATIONS

[1] van 't Hoff Institute for Molecular Sciences, University of Amsterdam, P.O. Box 94157, 1090 GD Amsterdam, The Netherlands
[2] Institute of Physics, University of Amsterdam, P.O. Box 94157, 1090 GD Amsterdam, The Netherlands

[a)] **Author to whom correspondence should be addressed:** p.g.bolhuis@uva.nl

ABSTRACT

Synthetic colloidal patchy particles immersed in a binary liquid mixture can self-assemble via critical Casimir interactions into various superstructures, such as chains and networks. Up to now, there are no quantitatively accurate potential models that can simulate and predict this experimentally observed behavior precisely. Here, we develop a protocol to establish such a model based on a combination of theoretical Casimir potentials and angular switching functions. Using Monte Carlo simulations, we optimize several material-specific parameters in the model to match the experimental chain length distribution and persistence length. Our approach gives a systematic way to obtain accurate potentials for critical Casimir induced patchy particle interactions and can be used in large-scale simulations.

I. INTRODUCTION

Advances in colloid chemistry have enabled the synthesis of micrometer-sized particles that, when immersed in a near-critical binary liquid mixture (e.g., water and lutidine), experience anisotropic directional interactions induced by a critical Casimir force. As such patchy particles can make directed bonds, i.e., only one bond per patch, they can be viewed as mesoscopic analogs of (carbon) atoms.[1] Their micrometer-sized scale makes them directly observable via a confocal microscope, while they simultaneously still experience thermal motion that lets them obey the same statistical behavior of molecules and atoms, i.e., the Boltzmann distribution. Hence, colloidal patchy particles are well suited as an experimental model system to explore complex structures analogous to molecular architectures. Indeed, by exquisite temperature control of the Casimir interaction, patchy particles can form colloidal architectures, such as chains and rings, revealing molecular-like structures.[2,3]

Much experimental work has been performed on the self-assembly of patchy particles,[4–7] and many computer simulations have investigated generic static and dynamic properties.[8–15] However, most common colloidal interaction models cannot reproduce or predict experimental observation because this behavior is sensitive to the precise form of the effective interactions at the experimental conditions, as dictated by the material and solvent properties.

In this work, we aim to develop an accurate model for patchy particle systems that can quantitatively predict the outcome of experiments. Such models would have several advantages. First, it would be possible to mimic the experimental setup and understand what is happening on the particle level, e.g., the conformational ring statistics in Ref. 3. As such, simulations bring structural and dynamical insight into the experimental observations. Second, accurate potentials used in a multi-scale simulation provide large-scale and long-time behavior, enabling the exploration of new hypotheses. Moreover, such simulations will serve as a predictive tool and provide a guide to design future experiments. Finally, our work shows a systematic road toward the development of accurate effective patchy particle potentials.

While in previous work,[16] we developed a potential for (experimental) dumbbell particles where two sites are both interacting isotropically, here we focus on spherical particles with directional patches. In the experimental realization of the system, a small patch is exposed at the surface of a colloidal particle made of a different

material. The specific wetting properties of the patch and the colloidal particle material with respect to the two components of the near-critical liquid mixture induce the Casimir interactions between the patches.[17–19]

The model we develop for simulating patchy colloidal particles is based on theoretical (isotropic) pair potentials valid for spherical colloidal particles immersed in an off-critical binary liquid. The Yukawa potential describes the repulsive part, and the attractive part originates from the critical Casimir interactions.[20,21] As the theoretical potentials are constructed for a particle with a radius matching the radius of curvature of the patch on the patchy particle of interest, we assume prior knowledge of its geometry. Additionally, these isotropic potentials depend on properties of the solvent and the colloidal particle and contain two imprecisely known parameters: the surface charge density and the wetting scaling parameter.

Next, we model the patches of the colloidal particle by multiplying the isotropic interaction by a switching function, which decays from one to zero, interpolating between a fully bonded and a nonbonded configuration, depending on the relative orientations of the interacting patches. The precise form of this switching function is computed by performing an explicit numerical integration over the two patch surfaces at various orientations.

As there are several unknown parameters in the theoretical potentials, it is not easy to come up with an entirely bottom-up approach. Therefore, we adopt a hybrid top-down/bottom-up procedure and parameterize the potential by benchmarking it on experimental measurements.

Implementing the full potential for a colloidal dipatch particle system, we performed extensive Monte Carlo (MC) simulations for colloidal systems under gravity. As expected, the particles assemble into chains for sufficiently strong attraction and we measure the persistence length and chain length distributions at various temperatures (Fig. 1). The potential is then matched to mimic the experimental results by tuning the surface charge density, scaling wetting parameter, and patch size.

The remainder of the paper is organized as follows. In Sec. II, the patchy particle model is presented, which is based on the physical dimensions of the patchy particle, theoretical critical Casimir interactions, and electrostatic repulsion; Sec. III shows details of the simulated system to calculate the chain length distributions and persistence lengths; and in Sec. IV, we show the effects of the fitting parameters on the two observables and the optimization of the potential. We end with concluding remarks.

II. THEORETICAL BACKGROUND

Following the bottom-up approach, we start with introducing the pair potential of isotropic particles immersed in a binary liquid, followed by the pair potential of patchy particles. Then, by adding the external gravitational field, the full potential is constructed.

Next, we apply our general model onto the dipatch particle system that is based on physical dimensions of the experimentally measured particles.

A. The isotropic pair potential

The isotropic pair potential is based on the work of Stuij *et al.*,[21] which presented a model for the attractive critical Casimir potential between two spherical colloidal particles immersed in an off-critical binary liquid. The model is constructed by mapping experimentally measured radial distribution functions and second virial coefficients onto pair potentials based on critical Ising model Monte Carlo simulations and mean-field theoretical methods.[23]

These isotropic potentials $V_{\text{isotropic}}$ are composed of the repulsive Yukawa potential V_{Yukawa} and the attractive critical Casimir potential obtained from the theoretical scaling function $V_{\text{C}}^{\text{theory}}$. Their isotropic nature makes them a function of the interparticle distance r only,

$$V_{\text{isotropic}}(r) = V_{\text{Yukawa}}(r) + V_{\text{C}}^{\text{theory}}(r). \tag{1}$$

The potential V_{Yukawa} describes the screened Coulomb repulsion between the colloidal particles in a polar solvent. It is a coarse-grained model that captures the screening effect of the electric double layer of the ions in the solvent.[24,25] The Yukawa potential of two identical charged particles with diameter σ_c and center-to-center

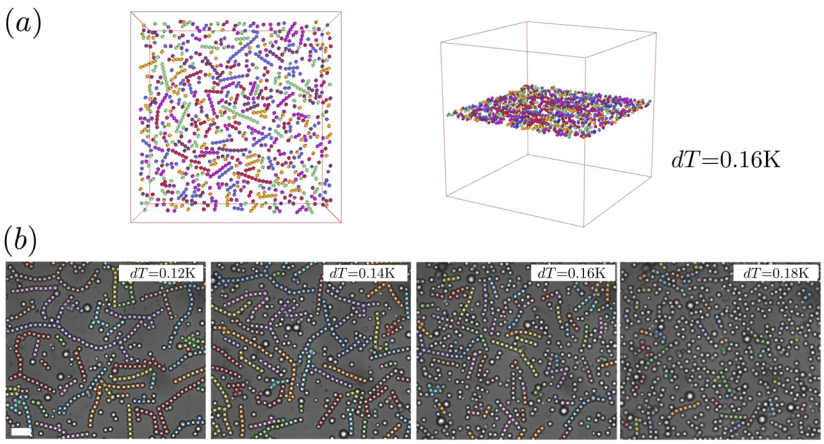

FIG. 1. (a) Top and side view from the simulation box at dT = 0.16 K. (b) Snapshots from experiment at various temperatures.[22] Distinct chains are indicated by the colors.

distance r apart is

$$V_{\text{Yukawa}}(r) = \begin{cases} \infty, & r \le \sigma_c, \\ U_0 \exp(-\kappa(r-\sigma_c))\sigma_c/r, & r > \sigma_c, \end{cases} \quad (2)$$

with

$$U_0 = \frac{Z^2 \lambda_B}{(1+\kappa\sigma_c/2)^2 \sigma_c}, \quad (3)$$

where $Z = \pi\sigma_c^2 \Upsilon$ is the charge of the particles, Υ is the surface charge density, $\lambda_B = \beta e^2/4\pi\epsilon$ is the Bjerrum length of the solvent with ϵ is the permittivity of the solvent, e is the elementary charge, and $\beta = 1/k_B T$ is the inverse temperature with k_B the Boltzmann constant. The screening length, i.e., Debye length, is defined as $\kappa^{-1} = \sqrt{\epsilon k_B T/e^2 \sum_i \rho_i}$ where ρ_i is the number density of monovalent ions in the solvent.[26]

The attraction is caused by critical Casimir interactions resulting from the diverging bulk correlation length ξ of the concentration fluctuations of a binary solvent near its critical point. The surfaces of two spherical particles, or differently shaped objects such as walls, patchy particles, or cubes,[27–30] act as boundary conditions (BCs) confining the fluctuations between them. When the distance between the objects becomes smaller than ξ, the spatial restriction on the critical fluctuations gives rise to an effective force, called critical Casimir force, first introduced by Fisher and de Gennes in 1978.[31] This effective force is attractive or repulsive depending on the identical or opposing surface preference of the BCs. In the theoretical description, this surface preference is captured by the so-called surface field h_s that depends on a material-specific (dimensionless) wetting parameter w, i.e., the hydrophilic or hydrophobic affinity of the surface with the solvent.[29,32,33]

The critical Casimir interaction between two spheres of radius R_p follows a universal scaling function $\hat{\Theta}$ according to finite-size scaling theory (see Appendix A),

$$V_C^{\text{theory}}(r) = \frac{w^3 R_p}{D} \hat{\Theta}^{(d=3,\text{Derj})}(\mathcal{Y}/w, \Lambda), \quad (4)$$

where distance $D = r - 2R_p$ and r is the interparticle distance of the two particles with radius R_p. This form holds for two spheres with $R_p \gg D$, in the Derjaguin approximation in three dimensions ($d = 3$).

The first variable in the scaling function $\mathcal{Y} \equiv \text{sgn}(t) D/\xi_t$ is dependent on the scaled temperature $t = (T_c - T)/T_c$ with T_c as the critical temperature and T as the temperature, and the solvent correlation length is $\xi_t \equiv \xi_{t,\pm}^{(0)} |t|^{-\nu}$ along the path $t \to 0^{\pm}$ at the critical composition. The second variable in the scaling function $\Lambda \equiv \text{sgn}(h_b) D/\xi_h$ depends on the bulk ordering field h_b. The bulk ordering field is proportional to the difference between the chemical potentials of the solvent species A and B such that $h_b \sim \mu_A - \mu_B - (\mu_A - \mu_B)_c$ with respect to the critical point. The related solvent correlation length is $\xi_h = \xi_h^{(0)} |h_b|^{-\nu/\beta\delta}$ along the path $h_b \to 0$ with $t = 0$.

While the scaling exponents ν, β, δ, and the amplitude ratio $\xi_{t,+}^{(0)}/\xi_{t,-}^{(0)}$ are universal,[34] the magnitude of the amplitudes of $\xi_{t,\pm}^{(0)}$ and $\xi_h^{(0)}$ is not.

The universal scaling behavior means that the critical Casimir interactions are largely independent of microscopic details of the system but are instead a function of the thermodynamic state of the solvent and the properties of the boundary conditions. The former includes the composition of the binary liquid c, salt concentration c_{salt}, and phase separation temperature T_{cx}, where the latter is a function of the radius R_p of the particle and scaling wetting parameter w.

B. The patchy particle pair potential

For the construction of the patchy particle pair potential, consider a patchy particle that consists of a spherical bulk particle of diameter $\sigma = 2R$ with n_p spherical patch particles with radius R_p, located such that the patch particle cuts through the surface of the bulk particle, yielding an exposed circular patch of diameter d_p [see Fig. 2(a)].

Due to the short nm-ranged character of the critical Casimir interaction, which is at least an order of magnitude smaller than the particle diameter, only a small area of the exposed patch surfaces interacts. While in principle there is also a bulk–bulk Casimir attraction, this is relatively weak compared to the patch–patch attraction and will be dominated by the repulsive electrostatic potential at the experimentally chosen conditions. We can therefore neglect these interactions. Note that the situation would be reversed for compositions on the other side of the critical composition.

Suppose two patchy particles are facing each other at their minimum energy position. In that case, the bulk particle and the edges of the circular patch surface do not contribute to the effective interaction calculated in the Derjaguin approximation, as this

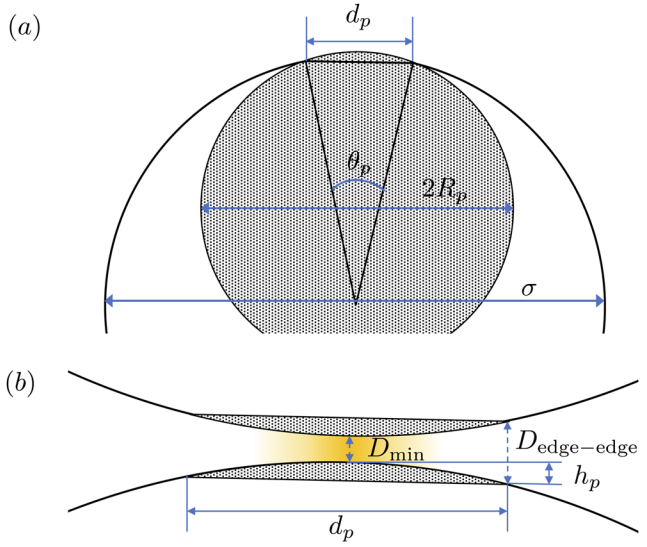

FIG. 2. (a) The computational patchy particle is composed out of two components: the bulk colloidal particle (white circle) and the patch colloidal particle (dotted circle). (b) Schematic illustration zoomed in at the bond of two patchy particles. If θ_p is large enough, $D_{\text{edge-edge}}$ falls outside the range of $V_{\text{isotropic}}$ and only a small fraction of the patch surfaces interacts, as illustrated with the yellow color. The patch height h_p, the projected patch diameter d_p, the patch surface–surface distance D_{min} and $D_{\text{edge-edge}}$ are indicated (dotted lines).

distance $\geq D_{\text{edge-edge}}$ [see Fig. 2(b)] falls outside the range of the critical Casimir interaction. Therefore, the effective interaction between two facing patches of two particles is accurately approximated by the isotropic pair potential [Eq. (1)] of two spherical particles with radius R_p.

The pair interaction V_{pair} between the patchy particles arises from the electrostatic repulsion V_{Yukawa} and the patch–patch attractive interaction,

$$V_{pair}(r_{ij}, \Omega_i, \Omega_j) = V_{\text{Yukawa}}(r_{ij}) + \min_{1\leq k,l\leq n_p} V_{\mathbf{p}_{ik},\mathbf{p}_{jl}}(r_{ij}, \Omega_i, \Omega_j) \quad (5)$$

where the min function gives the minimum energy of the set of all possible patch–patch potentials. The position of each patch in the particle reference frame is given by n_p unit vectors $\mathbf{p}$ that point from the particle's center to the center of the patch. This mimics the fact that only one bond per particle pair can be formed. This patch–patch potential $V_{\mathbf{p}_{ik},\mathbf{p}_{jl}}$ is defined as

$$V_{\mathbf{p}_{ik},\mathbf{p}_{jl}}(r_{ij}, \Omega_i, \Omega_j) = V_C^{\text{theory}}(r_{ij}) S_{\mathbf{p}_{ik},\mathbf{p}_{jl}}(\Omega_i, \Omega_j), \quad (6)$$

where $V_C^{\text{theory}}(r_{ij})$ is the (isotropic) critical Casimir attraction for two particles with diameter $2R_p$ given in Eq. (4). The switching function $S_{\mathbf{p}_{ik},\mathbf{p}_{jl}}(\Omega_i, \Omega_j)$ captures the effective interaction strength as a function of particles' orientation Ω (given by a quaternion representation). The strongest bond is formed if the patches are aligned, as illustrated in Fig. 2(b), yielding $S = 1$. The bond weakens when patches are rotated away, rendering $S \in [0, 1\rangle$.

C. The switching function

This switching function is in principle six-dimensional (three degrees of freedom for each orientation Ω). However, by making use of the symmetry of the system, it reduces to three dimensions. To do so, we define three angles θ_i, θ_j, and θ'_{ij} and a distance r to represent all conformations that two particles can have when making a bond. In Fig. 3 on the left, the θ_i and θ_j angles are illustrated. They are defined as

$$\cos(\theta_i) = \frac{\mathbf{p}_{ik} \cdot \mathbf{r}_{ij}}{|\mathbf{p}_{ik}||\mathbf{r}_{ij}|}, \quad -\cos(\theta_j) = \frac{\mathbf{p}_{jl} \cdot \mathbf{r}_{ij}}{|\mathbf{p}_{jl}||\mathbf{r}_{ij}|}, \quad (7)$$

where $\mathbf{p}_{ik}$ ($\mathbf{p}_{jl}$) is the kth (lth) patch vector of particle $i(j)$ and $\mathbf{r}_{ij} = \mathbf{r}_j - \mathbf{r}_i$ is the interparticle center-to-center distance vector. The angle θ'_{ij} is defined as the patch vectors' projected angle on the plane perpendicular to the interparticle vector, as illustrated in Fig. 3 on the right. Note that by aligning the reference frame with $\mathbf{r}_{ij}$, we can make this representation rotationally and translationally invariant. In this way, the six-dimensional function $S_{\mathbf{p}_{ik},\mathbf{p}_{jl}}(\Omega_i, \Omega_j)$ is reduced to a three-dimensional function $S(\theta_i, \theta_j, \theta'_{ij})$.

The function $S(\theta_i, \theta_j, \theta'_{ij})$ can be computed by a numerical integration of the effective attractive critical Casimir interaction at various conformations defined by θ_i, θ_j, and θ'_{ij}. To simplify the integration, the patch curvature is set equal to the curvature of the bulk particle. In Appendix B 3, we show that the integrated function $S(\theta_i, \theta_j, \theta'_{ij})$ can be well approximated by

$$S(\theta_i, \theta_j, \theta'_{ij}) \approx S'(\theta_i) S'(\theta_j), \quad (8)$$

where $S'(\theta_i)$ depends only on one angle and is a fit of the part of the integrated $S(\theta_i, \theta_j, \theta'_{ij})$ where one of the particles is fixed at $\theta_j = 0°$, while the other is rotated by $\theta_i \geq 0°$,

$$S'(\theta) = \exp\left(\sum_{l=2}^{8} c_l \theta^l\right). \quad (9)$$

In a self-assembled patchy particle dispersion, the persistence length and distribution of the chain lengths are not strongly affected by the choice of the definition of S by either θ_i, θ_j, and θ'_{ij} or making the simplification of only incorporating θ_i and θ_j as in Eq. (8). See Appendix B 3 for more details.

D. The external potential V_{gravity}

To mimic the experimental observation that patchy particles tend to sink to the bottom of the sample due to the gravitational force F_g pulling the colloids down, we add an external gravitational potential to the model. The gravitational potential V_g,

$$V_g(z) = \Delta m g z = -F_g z, \quad (10)$$

depends on gravitational acceleration (on Earth in this case) g, height z, and mass difference Δm between the patchy particle and the solvent (see Appendix B 2 for details).

The bottom of the sample is mimicked by a steep Lennard-Jones 12-6 potential (V_{LJ}), which is connected to V_g at the transition point z_{cut} with an equal first derivative,

$$V_{\text{LJ}}(z_{\text{cut}}) = V_g(z_{\text{cut}}), \quad (11)$$

$$V'_{\text{LJ}}(z_{\text{cut}}) = V'_g(z_{\text{cut}}). \quad (12)$$

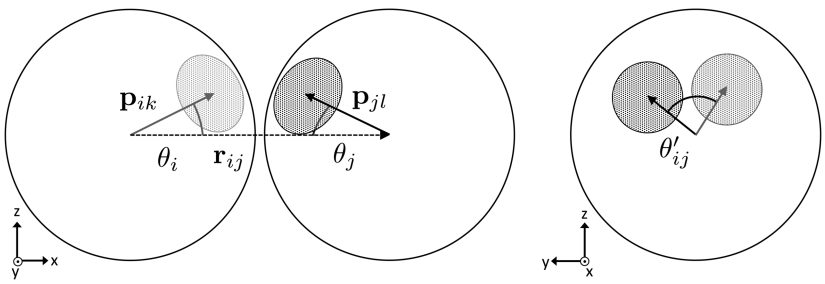

FIG. 3. Two single patch particles with their interparticle vector $\mathbf{r}_{ij}$ (dotted arrow) and patch vectors $\mathbf{p}_{ik}$ and $\mathbf{p}_{jl}$ (solid arrows). The light and dark gray colored patches are behind and in front of the plane of the paper, respectively. The angles θ_i, θ_j, and θ'_{ij} are indicated with a bow.

The complete external potential is thus

$$V_{\text{gravity}}(z) = \begin{cases} V_{\text{LJ}}(z), & z \le z_{\text{cut}}, \\ V_g(z), & z > z_{\text{cut}}, \end{cases} \tag{13}$$

$$= \begin{cases} 4\epsilon_{\text{LJ}}\left(\frac{\sigma}{z}^{12} - \frac{\sigma}{z}^{6} + \frac{1}{4}\right), & z \le z_{\text{cut}}, \\ -F_g z - b, & z > z_{\text{cut}}, \end{cases} \tag{14}$$

where ϵ_{LJ} is a self-chosen value. This potential is smooth up to the first derivative and is suited for molecular dynamics as well as Monte Carlo simulations.

E. The system's potential energy

The full potential of N spherical colloidal patchy particles interacting via the effective pair potential V_{pair} and experiencing a gravitational field is given by a summation over the pair potentials between all pairs of patchy particles,

$$V = \sum_{i<j}^{N} V_{pair}(r_{ij}, \Omega_i, \Omega_j) + \sum_{i}^{N} V_{gravity}(z_i), \tag{15}$$

and the external field $V_{gravity}$ caused by the gravity and the cell boundary. The latter is only dependent on z, the vertical component of the particle's position.

F. Constructing the dipatch particle potential

So far the described a model is generally applicable onto patchy particles interacting via critical Casimir interactions and electrostatic repulsions under a gravitational field. However, the model still contains two material-specific parameters: w (wetting parameter) and Υ (surface charge density). Since these are not precisely known, they are treated as free parameters to optimize our potential model using experimental data. We stress here that these parameters are not meaningless fit parameters but have a physical meaning, and their range of possible values is thus limited.

The dipatch particles of interest from Refs. 2 and 22 are immersed in a water–lutidine (75/25 vol. %) solution with c_{MgSO_4} = 1.0 mM. The ions not only screen the surface charge and affect the electrostatic repulsion but also allows one to tune specific patch–patch interactions.[35–37] The physical dimensions of these dipatch particles are measured with AFM (atomic force microscopy).[22] The particle's diameter σ, projected patch diameter d_p, patch arc-angle θ_p, patch height h_p, and R_p are listed in Table I and indicated in Fig. 2.

The parameters of the repulsive Yukawa potential [Eqs. (2) and (3)] of this solution are κ^{-1} = 2.78 nm, ϵ = 2.25 $\times 10^{-10}$ F/m,[17] λ_B = 2.14 nm, and $\sigma_c = 2R_p$. The surface charge density Υ remains a fitting parameter.

TABLE I. The particle diameter σ, projected patch diameter d_p, patch arc-angle θ_p, patch height h_p, patch radius of curvature R_p are measured with AFM. The number in brackets indicates the standard deviation of the last digit based on four measurements.

σ (μm)	d_p (μm)	θ_p (°)	h_p (nm)	R_p (μm)
3.2(1)	0.58(5)	21(2)	45(5)	1.0(2)

TABLE II. Critical Casimir non-universal and universal scaling constants (from Refs. 21 and 34).

$\xi_{t,+}^{(0)}$ (nm)	$\mathcal{B}$	ν	β	δ
0.198	0.765	0.63	0.3265	4.789

In an off-critical binary liquid, instead of measuring t, the off-set $dT = T_{cx} - T$ from the phase separation temperature T_{cx} is measured.

For the construction of the potentials, the location of T_c with respect to T_{cx} is calculated with the relation $\frac{T_{cx}-T_c}{T_c} = \left(\frac{c_c - c}{\mathcal{B}}\right)^{1/\beta}$ where c_c = 0.287 denotes the critical (lutidine mass) fraction,[38] $\mathcal{B}$ is a non-universal scaling constant of the water lutidine solution without salt measured in Ref. 39, and β is a universal scaling constant (see Table II).

V_C^{theory} is obtained as numerical data from Ref. 21 using the universal and non-universal scaling parameters listed in Table II. For our simulations, it is convenient to have an analytical expression and analytical interpolation of the numerical data. The data are well represented by the following functional form:

$$V_C(r; dT, w) = -\frac{A}{B}\exp\left(-\left(\frac{r-\sigma}{B}\right)^2\right), \tag{16}$$

which we fit as functions of wetting scaling factor $w \in [0.40, 0.56]$ and $dT \in [0.12, 0.22]$ K, which is the temperature range of the experimental measurements. The resulting parameters $A(dT, w)$ and $B(dT, w)$ turn out to be well represented by the product of two simple cubic polynomials of the arguments (see Appendix B 1).

In order to set the effective patch–patch interaction equal to the isotropic pair potential of two patch particles, the critical Casimir attraction V_C^{theory} at distance $D_{\text{edge-edge}}$ should become negligible [see Fig. 2(b)]. Three potentials are shown in Fig. 4 using the above-described system, at various values for w with $\Upsilon = -0.15\ e/\text{nm}^2$ and

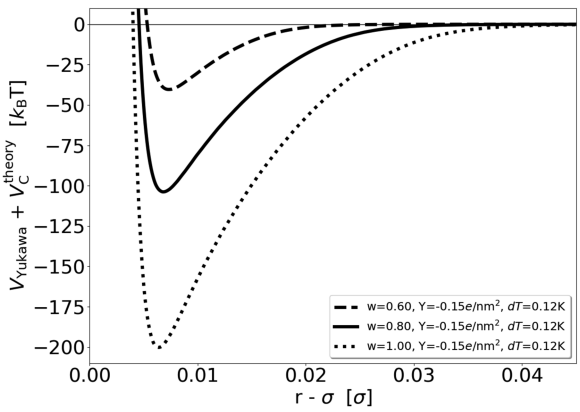

FIG. 4. Three pair potentials of two isotropic hydrophobic particles with radius R_p immersed in a water–lutidine (75/25 vol. %) solution with 1.0 mM $MgSO_4$ with $\Upsilon = -0.15\ e/\text{nm}^2$ and w = 1.00, 0.80, and 0.60 at dT = 0.12 K. All potentials become negligible at 0.035σ; thus, $V_{\text{pair}}(\theta_i = \theta_j = 0°) = V_{\text{isotropic}}$.

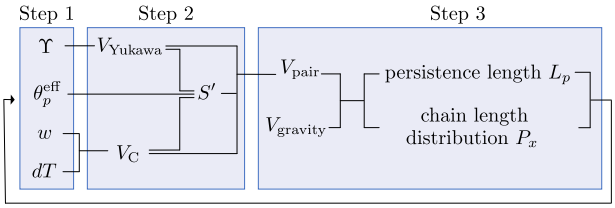

FIG. 5. Three-step calculation scheme for optimizing the patchy particle potential. The solid lines represent the dependencies, e.g., V_{Yukawa} is only dependent on Υ.

dT = 0.12 K. Even at maximum value w = 1.00, when the interaction depth reaches ~−200 $k_{\text{B}}T$, the interaction strength at 0.035σ ($D_{\text{edge-edge}} = 2h_p + D_{\text{min}}$) is negligibly small. The potential with w = 0.60, which has a more realistic interaction strength, becomes negligibly small at 0.025σ. Thus, if the bonds are aligned, i.e., $\theta_i = \theta_j$ = 0°, then $V_{\text{pair}} = V_{\text{isotropic}}$.

If the patches rotate, a repulsive bulk–patch interaction arises due to opposing boundary conditions of the surfaces.[19] As this bulk–patch interaction distance (for $\theta \to 0°$ at $D_{\text{edge-edge}}$) is longer than the attractive interaction distance 0.025σ, we assume this repulsive contribution to be small compared to the attraction and ignore it in the description of the potential. Nevertheless, to compensate for this assumption, a smaller effective patch width θ_p^{eff} than the experimental θ_p is allowed. This approach circumvents the explicit calculation and benchmark of the repulsive contribution, which would introduce more unknown parameters to the model.

We employ a three-step calculation scheme, as illustrated schematically in Fig. 5, for benchmarking the experimental measurements to the model. We start with defining the four input parameters: Υ, w, dT, and θ_p^{eff}. In the second step, from the former three input parameters, the isotropic potentials V_{Yukawa} and V_{C} are constructed, and, in combination with the latter, the part $S'(\theta)$ of the angular switching function S in Eq. (8) is determined by numerical integrating. Next, by employing MC simulations, the persistence length L_p and chain length distribution P_x are measured using V_{pair} and V_{gravity}. Finally, based on L_p and P_x over the whole temperature range, the input parameters Υ, w, and θ_p^{eff} are adjusted, and the steps are repeated.

To perform this adjustment efficiently, we first illustrate the effect of the input parameters on V_{pair} with five example potentials with dT = 0.12–0.22 K (Fig. 6). Later in Sec. IV A, their qualitative

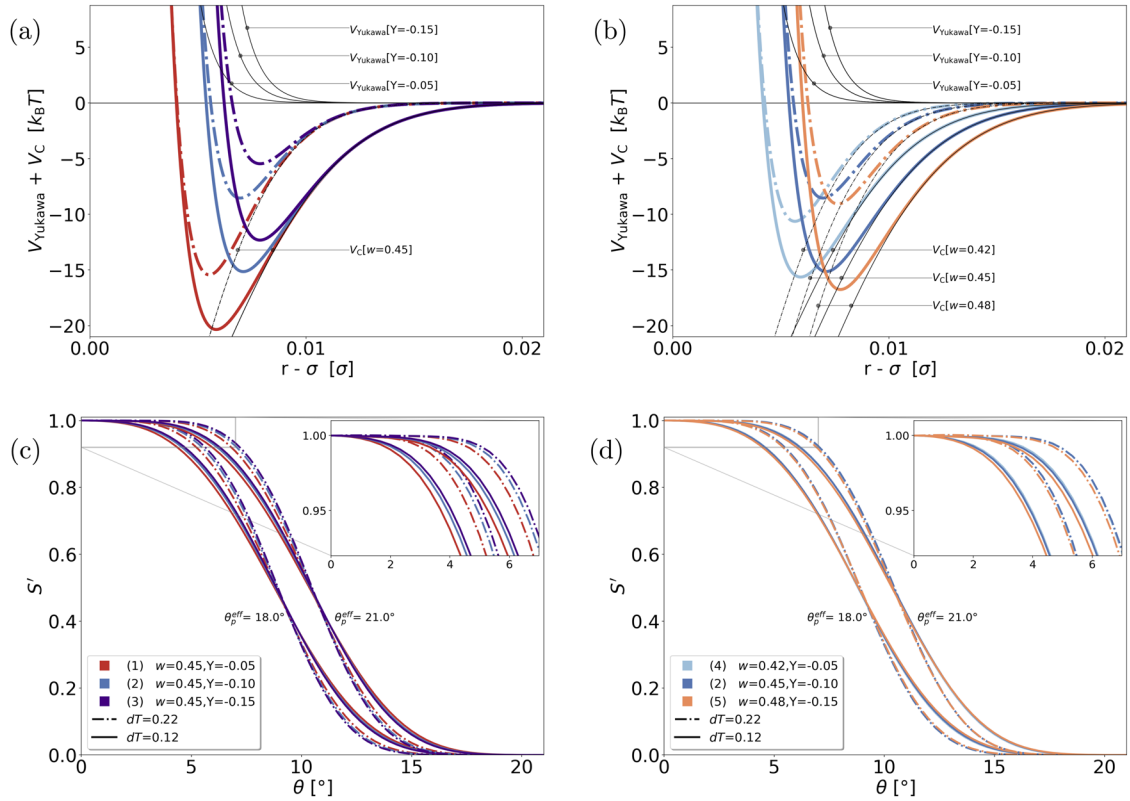

FIG. 6. Pair potentials of the dipatch particles with diameter σ dressed with hydrophobic patches with radius of curvature R_p, immersed in a water–lutidine (75/25 vol. %) mixture with 1 mM $MgSO_4$. [(a) and (b)] Radial parts, V_{Yukawa} and V_{C}. [(c) and (d)] Corresponding switching functions S′ with θ_p^{eff} = 18.0 and 21.0°. The w and Υ(Υ) combinations are indicated by the numbers (1)–(5) and the color coding, and the lines indicate dT = 0.12 K (solid) and dT = 0.22 K (dashed-dotted).

effect on absolute values and temperature trends on L_p and P_x is demonstrated.

Decreasing Υ, i.e., making it more negative, makes the repulsion V_{Yukawa} stronger and, therefore, the pair potential weaker [Fig. 6(a)]. Although S' is based on the change of the effective attractive interaction, the repulsion plays a role in the location of the minimum, and thus, also Υ has an effect on S' [Fig. 6(c)].

As the scaling function $\hat{\Theta}$ is multiplied by w^3 and the correlation length ξ_t by w, increasing w will make V_C effectively deeper and its interaction range longer. The resulting switching function S' becomes more narrow around $\theta \sim 5°$ and less steep around 10° (not explicitly shown in Fig. 6).

If both w and Υ are adjusted simultaneously, potentials with similar interaction strength can be created, but with a different temperature dependence [Fig. 6(b)]. For example, by comparing potentials (4) and (5), the minima of (4) at $dT = 0.12$ and 0.22 K are closer together than (5). This means that there is a weaker temperature effect in (4) compared to (5). Adjusting w and Υ simultaneously can therefore serve as a knob to adjust the effective temperature dependence of V_{pair}.

Finally, if θ_p^{eff} is decreased, e.g., from 21.0° to 18.0°, the curvature of the switching function S' shifts with a constant to smaller angles, while the curvature itself stays the same. Note that the assumption $V_{\text{isotropic}}(D_{\text{edge-edge}}) \approx 0 k_B T$ should still hold upon making θ_p^{eff} smaller, else a discontinuity in the force around $\theta = 0°$ appears.

III. SIMULATION METHODS

A. Monte Carlo simulation of the chain length distribution

For the chain length distribution simulations, a cubic box of length 51.17σ with 1000 particles with periodic boundary conditions, corresponding to an area fraction of $\eta = \rho\pi/4 = 0.30$, where ρ is the number density, is simulated with Monte Carlo (MC). Starting from a random configuration, the system was equilibrated by performing between 1×10^4 up to 6×10^4 MC cycles for the weak and strong interaction strengths, respectively. Each MC cycle consists of 5×10^5 single particle (95%) and cluster moves (5%).

In a single particle move, a randomly selected particle is either rotated (50%) or translated (50%) and can create and break bonds. Note that even though the potentials are deep, breakage occurs. In the case of the strongest potential, we observe typically thousands of bond breakage events. The rotation is performed using a random quaternion with an angle uniformly chosen $\in [0, dq_{\max}]$. The translation is performed using a random vector $\vec{r}$ with length uniformly chosen $\in \left[0, \sqrt{3} dr_{\max}\right]$. To enhance the decorrelation and make the sampling in the quasi-2D x,y-plane more efficient, the z-component of the translation vector $\vec{r}$ is reduced by a factor of 10 to avoid the particle being placed outside the quasi-2D plane, i.e., inside the wall or far above the gravitational height.

For the cluster move, the translation or rotation move is performed on a chain that is composed of particles that are connected via bonds, i.e., the attractive term in the pair potential is negative, or on single particles. Detailed balance is obeyed by keeping the number of clusters constant. Therefore, any new configuration that creates a new bond is rejected.

The maximum displacement $dr_{\max}$ and maximum rotation $dq_{\max}$ of the single particle and cluster moves are adjusted to maintain an acceptance ratio between 30% and 70%.

Measurements are performed on three independent samples during 7×10^4 MC cycles. The chain length distribution is calculated as $P_x = \frac{n_x}{\sum_i n_i}$ with P_x being the probability of a chain of length x, n_x being the number of chains with length x, and $\sum_i n_i$ being the total number of chains.

B. Measuring the persistence length

The persistence length L_p is calculated via a mode analysis of the chain in the worm-like chain model, in the same manner as done for the experimental measurement.[2] For a chain fluctuating in a two-dimensional plane, the variance of the mode amplitudes is related to the persistence length via

$$\left\langle (a_n - \langle a_n \rangle)^2 \right\rangle = \frac{2}{L_p} \left(\frac{L}{n\pi} \right)^2, \tag{17}$$

where a_n is the mode amplitude of mode number n and L is the contour length of the chain.[40,41]

To determine the mode fluctuations, we use MC runs to sample the conformation of a chain consisting of 15 dipatch particles in three independent samples, while not allowing bonds to break. To enhance decorrelation, in addition to single particle rotation and translation moves, tail flipping moves are performed. In this move, an interparticle bond vector $\vec{r}_{\text{bond}}$ of the chain is randomly selected. Then, all particles starting from $\vec{r}_{\text{bond}}$ to the tail end of the chain are rotated by 180° around $\vec{r}_{\text{bond}}$.

IV. RESULTS AND DISCUSSION

First, in Sec. IV A, we qualitatively compare the effects of the benchmark parameters w, Υ, and θ_p^{eff} on the chain length distribution P_x and persistence length L_p and identify three dependencies. In Sec. IV B, we perform the quantitative benchmark onto experimental measurements.

A. The P_x and L_p as a function of Υ, w, θ_p^{eff}, and dT

The three distinct dependencies become apparent in the chain length distributions in Fig. 7 and persistence length in Fig. 8 for potentials (1)–(5) from Fig. 6.

The first effect is that an increased radial potential strength leads to longer and stiffer chains over the complete temperature range. By comparing potentials (1)–(3), we observe increasing chain lengths, i.e., more longer chains, and stiffer chains for (3) < (2) < (1).

The second effect, that of shorter chains and stiffer chains over the complete temperature range, is achieved by reducing the effective patch width θ_p^{eff}. This effect is best observed in potential (2), which shows a strong reduction in chain lengths and a significant increase in the persistence length, but this holds for all potentials.

The third effect relates to the temperature dependence of P_x and L_p. By varying both w and Υ simultaneously, one can create potential with approximately equal strength, but with a different temperature dependence, as done for potentials (2), (4), and (5). By comparing

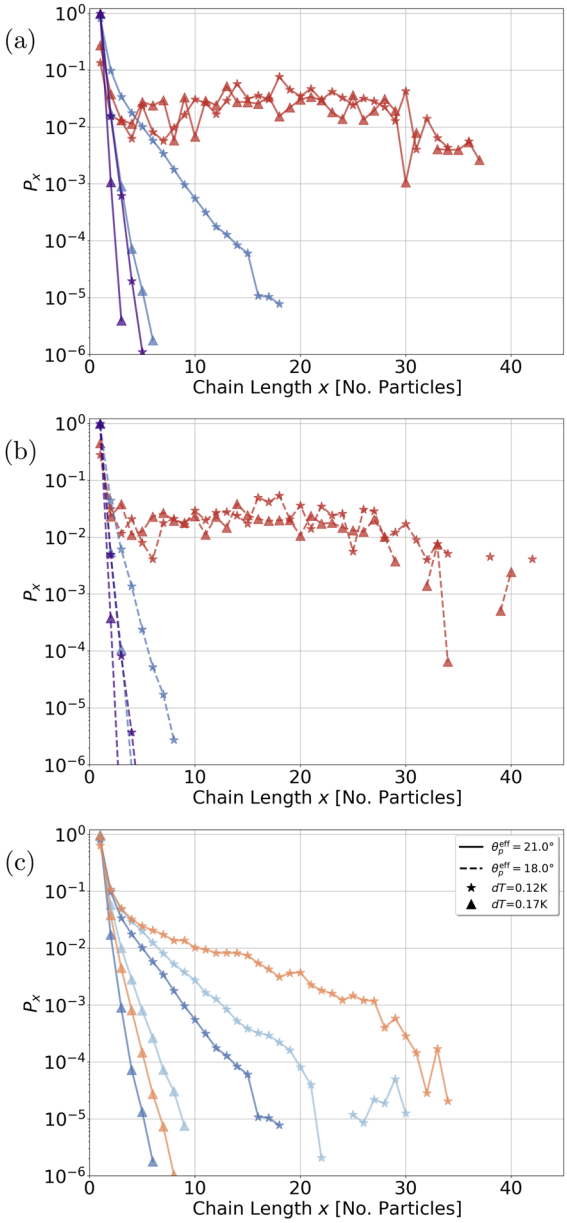

FIG. 7. Chain length distributions for potentials (1)–(3) with θ_p^{eff} = 21.0 (a) and 18.0° (b) and for potentials (2), (4), and (5) with θ_p^{eff} = 21.0° (c). The lines represent θ_p^{eff} and the symbols represent dT as indicated in the legend, while the color coding is from Fig. 6.

the chain lengths of potentials (4) and (5), at dT = 0.17 K, potential (4) shows the longest chains, while at dT = 0.12 K, it is potential (5) instead. Additionally, in the persistence length, the same temperature trend is observed, where at dT = 0.22 K the chain of potential (5) is more flexible than that of (4), while at dT = 0.12 K this is reversed. Thus, the temperature strength of the potentials can be tuned while still retaining similar chain lengths and flexibility.

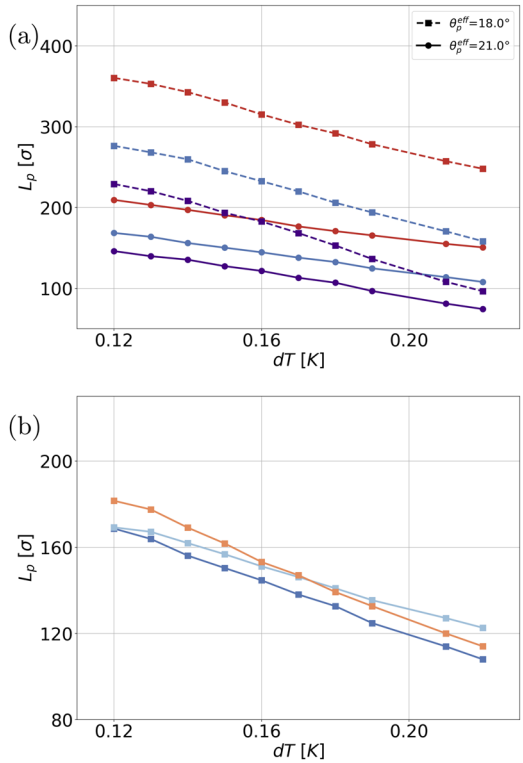

FIG. 8. Persistence length as a function of temperature of potentials (1)–(5). The effects of Υ and θ_p^{eff} (a) and combining Υ and w simultaneously (b) are shown. The line and symbol coding represents θ_p^{eff} as indicated in the legend, while the color coding is from Fig. 6.

B. Benchmarking P_x and L_p on experimental measurements

Now that we have examined the qualitative effects on P_x and L_p as a function of w, Υ, and θ_p^{eff}, we can benchmark the potential on the experimental measurements quantitatively. Two evaluation functions $R1$ and $R2$ are constructed that express the deviation of the simulation of L_p and P_x from the experiments, respectively.

For the persistence length measurements, $R1$ is defined as the percentage of deviation from the experimental values,

$$R1(L_p^{\text{exp.}}, L_p^{\text{sim.}}; dT) = \frac{L_p^{\text{sim.}} - L_p^{\text{exp.}}}{L_p^{\text{exp.}}} \cdot 100\% \tag{18}$$

and is calculated for each experimentally measured temperature dT = 0.12, 0.14, 0.16 K. Although not explicitly written, both $L_p^{\text{exp.}}$ and $L_p^{\text{sim.}}$ are, of course, temperature dependent.

Table III shows the evaluation of the persistence length of the chains for w = 0.456, 0.462, 0.470, Υ = −0.08, −0.09, −0.10 e/nm^2, and θ_p^{eff} = 19.0°, 19.5°, 20.0° for the three temperatures. For each combination of w and Υ, there exists a θ_p^{eff} in which the persistence length corresponds to experiment within ±8% indicated by the bold numbers.

In both experiments and simulations, we observe an increased monomer and dimer concentration, which does not coincide with

TABLE III. R1 [Eq. (18)] values that expresses the percentual deviation of the simulation from experiment. The bold numbers indicate the optimal θ_p^{eff} at given w and Υ.

	w	0.456			0.462			0.470		
Υ	θ_p^{eff} / dT	19.0	19.5	20.0	19.0	19.5	20.0	19.0	19.5	20.0
	0.12	**−5.5**	−13.3	−19.6	**−1.2**	−9.3	−16.5	5.8	**−3.0**	−11.3
−0.10	0.14	**0.2**	−7.6	−14.8	**4.9**	−3.3	−10.8	12.5	**2.6**	−5.6
	0.16	**0.4**	−6.9	−14.3	**5.6**	−3.1	−11.0	11.9	**3.5**	−5.3
	0.12	**−1.8**	−10.0	−17.5	2.8	**−5.4**	−13.4	8.4	0.1	**−7.9**
−0.09	0.14	**3.8**	−3.8	−11.7	10.3	**0.2**	−7.6	17.2	6.3	**−1.5**
	0.16	**4.9**	−3.4	−11.1	10.2	**1.2**	−7.0	17.3	7.9	**−1.1**
	0.12	2.3	**−6.0**	−14.0	8.0	**−1.6**	−9.9	14.6	4.5	**−4.3**
−0.08	0.14	9.6	**0.2**	−7.9	14.8	**4.9**	−3.1	21.9	11.4	**2.0**
	0.16	10.2	**1.4**	−6.6	15.3	**5.7**	−3.1	23.0	13.2	**3.2**

the expected exponential decay of the chain length distribution for longer chains (Fig. 9). Therefore, the simulated chain length distributions of chains with $x \geq 2$ are evaluated against fitted exponential curves of the (noisy) experimental data that exclude monomers and dimers. The deviation between the average of the three independent simulations and experiments is evaluated as

$$R2(P_x^{\text{R2}}, P_x^{\text{sim.}}; dT) = \frac{1}{x_{\max}} \sum_{x}^{x_{\max}} \left(\frac{P_x^{\text{sim}} - P_x^{\text{R2}}}{P_x^{\text{R2}}} \right)^2, \tag{19}$$

where P_x^{R2} is the experimental or fitted value. For each dT simulation, the sum runs over the chain lengths x up to $x_{\max}$, the maximum chain length for which holds $P_x \geq 5 \times 10^{-5}$ and length $x \leq 45$ particles.

Calculating chain length distributions requires more CPU time because there are more particles in the simulation box. Therefore, the chain length distribution simulations were only performed for the potentials with a good persistence length as listed in bold in Table III.

TABLE IV. R2 [Eq. (19)] value that expresses the deviation of simulation from experiment in order of magnitude. The bold values are from the selected potential.

w	0.456			0.462			0.470		
θ_p^{eff}	19.0	19.0	19.5	19.0	19.5	19.5	19.5	20.0	20.0
Υ	−0.10	−0.09	−0.08	−0.10	−0.09	−0.08	−0.10	−0.09	−0.08
dT									
0.12	0.60	0.51	0.09	0.52	**0.08**	2.69	0.24	7.13	9.69
0.14	0.61	0.57	1.60	0.54	**1.21**	39.52	9.25	143.09	804.29
0.16	0.63	0.57	0.12	0.57	**0.23**	$\sim 10^6$	0.14	$\sim 10^7$	$\sim 10^9$
0.18	0.54	0.54	0.43	0.55	**0.45**	50.59	0.33	$\sim 10^3$	$\sim 10^{20}$
0.22	0.48	0.45	0.55	0.45	**0.57**	0.40	0.56	0.32	0.07

Based on the smallest deviation from experiment over the whole temperature range as defined by $R1$ and $R2$ (indicated in bold in Table IV), the potential with $w = 0.462$, $\Upsilon = -0.090$ e/nm^2, and $\theta_p^{\text{eff}} = 19.5°$ is selected (Fig. 10). This optimized potential performs best in mimicking the experimentally measured temperature dependent chain length distribution and persistence length, as shown in Fig. 11.

Although the simulations still show small deviations from experiment, the potential cannot be significantly improved. For a truly perfect overlap, the potential should exhibit a weaker temperature dependence in P_x as the chains are too short at $dT = 0.22$ K and mimic experiment well at $dT = 0.12$ K, while it requires a stronger temperature dependence in L_p, as $R1$ shifts from positive ($dT = 0.22$ K) to negative ($dT = 0.12$ K). This is a contradicting property of the potential. Thus, changing the input parameters cannot lead to an improved potential, using the current potential forms.

We stress, however, that notwithstanding these small differences the potential model is remarkably accurate and can predict the assembly as well as the mechanical behavior over the relevant temperature range. Moreover, the final values for the free parameters

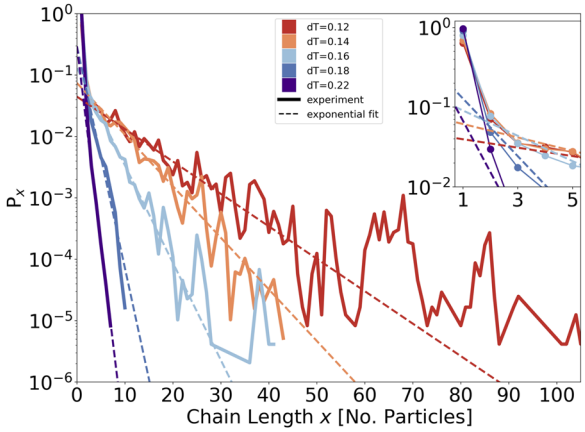

FIG. 9. The exponential fits onto the experimentally measured chain length distributions for $x > 2$ and $x \leq 55$, 30, 25, 10, and 8 for $dT = 0.12$, 0.14, 0.16, 0.18, and 0.22, respectively. The inset shows a zoom in which the connected dots by solid thin lines represent the experimentally measured probabilities for clarity.

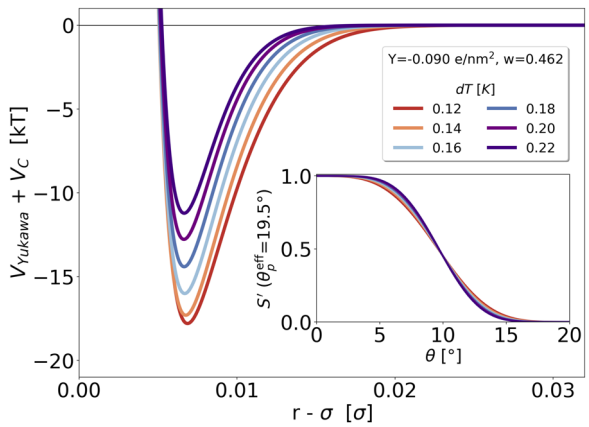

FIG. 10. The radial part of the pair potentials V_{Yukawa} and V_C and the switching function S' (in the inset) are shown for temperatures $dT = 0.12$–0.22 K with $w = 0.462$, $\Upsilon = -0.09$ e/nm^2, and $\theta_p^{\text{eff}} = 19.5°$.

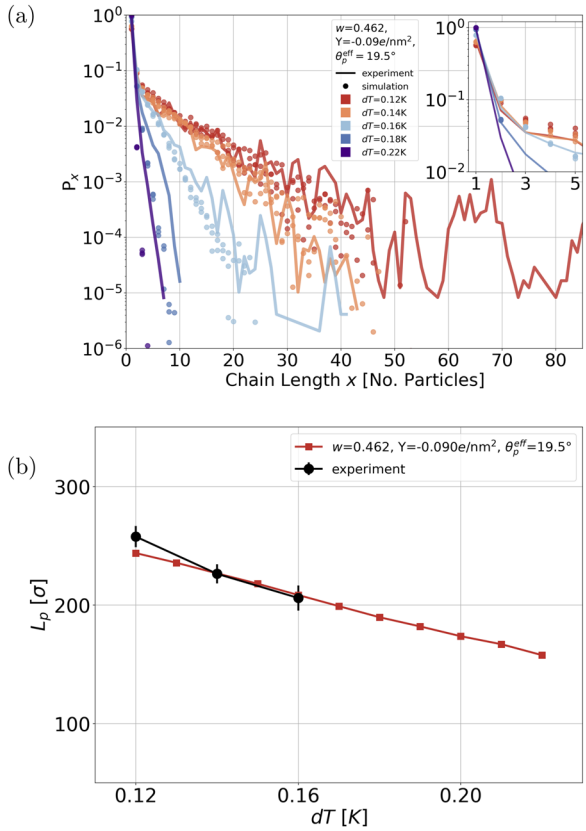

FIG. 11. With potential parameters $w = 0.462$, $\Upsilon = -0.090$ e/nm^2, and $\theta_p^{\text{eff}} = 19.5°$, the chain length distribution P_x (a) and persistence length L_p (b) are simulated and mimic experiment over the temperature range of $dT \in [0.12, 0.22]$ K. The vertical error bars in (b) represent the standard deviation of measurements consisting of 3600 images (30 min at a frame rate of 2 fps).

in the optimized model are physically reasonable. The patch angle θ_p^{eff} is very close to the measured patch width by AFM. The surface charge density is within the expected physical range for these types of colloids (see, e.g., Ref. 21). Finally, the optimal w value is lower than expected, but still reasonable. Thus, we conclude the potential model is physically sound and can be used for complex colloid systems.

V. CONCLUSION

In this work, we have developed an accurate potential model to simulate patchy particles interacting via critical Casimir forces. The potential model is based on a hybrid bottom-up/top-down coarse-graining approach, in which we take isotropic interaction from accurate scaling theory and adjust these to the patchy particle geometry, by numerical integration and fitting as a function of the patch orientation. While accurate, the theoretical scaling theory contains several poorly known material parameters, the wetting factor, the charge density, and the effective patch width. We optimized the potential by fine-tuning these parameters so that a system of these particles under gravitational field mimics the experimentally observed chain length distribution and persistence length as best as possible. Indeed, we demonstrated that the optimal potential model accurately predicts the experimental results.

While the optimization procedure might be seen as a fitting procedure, all parameters have a physical meaning, can be interpreted, and can only be used for fine-tuning. As there is basically no freely adjustable parameter, it is quite remarkable that we can simulate such a complex system accurately.

Thus, our work clearly shows how a single potential model can be developed to accurately simulate a complex system of patchy particles interacting with critical Casimir interactions, under a variety of conditions. Our approach provides a general framework to develop coarse-grained effective potentials that can be used to reproduce and interpret experiments and guide future experiment. For instance, a direct extension of the model is to describe multivalent patchy particles, e.g., tetra-patch particles, so that networks can be formed. Moreover, using the optimized potential model in a (Brownian) molecular dynamics setting can provide dynamical information.

We stress that our coarse-grained potential is naturally bound to a specific experimental system. Changing the system, will also change the potential. Therefore, the potential needs to be optimized for each new colloidal system. While this seems a drawback, we stress that much or our framework can be automatized. In fact, most of the effort will lie in the particle synthesis and collection of experimental data to benchmark the models.

Finally, we mention that our approach still relies on functional forms for the potentials and on standard fitting procedures. In the future, the use of machine learning can be considered to directly go from the theoretical isotropic potentials to the final model, without going through the intermediate fitting steps.

ACKNOWLEDGMENTS

The authors acknowledge the funding (Grant No. 680.91.124) of the Foundation for Fundamental Research on Matter (FOM), which is part of The Netherlands Organization for Scientific Research (NWO).

APPENDIX A: THE ISOTROPIC CRITICAL CASIMIR ATTRACTION

For the construction of the patchy particle potential, we start with the theoretical prediction for the isotropic critical Casimir interaction between two spheres with radius R_p, as described in Refs. 20 and 21. Here, for completeness, we outline the basics of this isotropic interaction. First, the scaling parameters are explained. Then, the mapping from $d = 4$ to 3 dimensions of the critical Casimir interaction between parallel plates is introduced, followed by the integration over two spheres in the Derjaguin approximation. For a more exhaustive overview on critical Casimir interactions, see Ref. 23, and for that on the construction of the isotropic potentials, see Ref. 21.

The critical Casimir force follows universal scaling functions determined solely by the universality classes of the solvent and of the colloid surfaces that are in contact with the binary liquid near its demixing transition.

An important determining factor in the critical Casimir force is the solvent correlation length ξ. This parameter ξ is a function of

its distance from the critical point at (T_c, c_c), i.e., temperature and concentration c_c. Specifically, it scales with the scaled temperature $t = (T_c - T)/T_c$ via $\xi_t = \xi_{t,\pm}^{(0)}|t|^{-\nu}$ with $t \to 0$ at the critical concentration and thus corresponds to the Ising model in the absence of an external magnetic field $\vec{B}$. The bulk ordering field h_b is proportional to the distance of the chemical potential μ of the off-critical mixture with respect to the critical chemical potential μ_c at c_c. The correlation length ξ scales as $\xi_h = \xi_h^{(0)}|h_b|^{-\nu/\beta\delta}$ with $h_b \to 0$ at $t = 0$. $\nu = 0.63$, $\beta = 0.3265$, and $\delta = 4.789$ are universal scaling exponents.[34]

The critical Casimir force is a function of scaled distances $\mathcal{Y}$ and $\Lambda = \mathrm{sgn}(h_b)\frac{D}{\xi_h}$ between the confining objects. During an experimental measurement, only t is easily varied, while h_b stays constant. Therefore, the scaling parameters are rewritten as

$$\mathcal{Y} = \mathrm{sgn}(t)\frac{D}{\xi_t} \qquad \Sigma = \frac{\Lambda}{\mathcal{Y}}. \tag{A1}$$

The critical Casimir interaction in three dimensions for two parallel plates is denoted $\vartheta_\parallel^{(d=3)}(\mathcal{Y}, \Sigma)$. This function is not directly known but is determined via mapping 3D MC Ising model simulations at $\Sigma = 0$, i.e., $h_b \to 0$, and $\vartheta^{(d=4)}(\mathcal{Y}, \Sigma)$ from mean-field theory within Landau–Ginzburg theory,[42]

$$\vartheta_\parallel^{(d=3)}(\mathcal{Y}, \Sigma) = \frac{\vartheta_\parallel^{(d=4)}(\mathcal{Y}, \Sigma)}{\vartheta_\parallel^{(d=4)}(\mathcal{Y}, \Sigma = 0)}\vartheta_\parallel^{(d=3)}(\mathcal{Y}, \Sigma = 0). \tag{A2}$$

The material-dependent surface–solvent interactions are dependent on the surface fields h_s.[33] Including the effect of h_s via $w(h_s)$ explicitly in $d = 4$ gives $\vartheta_\parallel^{(d=4)}(\mathcal{Y}, \Sigma; h_s) = w^d\vartheta_\parallel^{(d=4)}(\mathcal{Y}/w, \Sigma)$. It is assumed that this also holds for $d = 3$, although this has not been explicitly tested.

Using the force $F_{C,\parallel}(L) = SL^{-3}\vartheta_\parallel^{(d=3)}(L/\xi_t, \Sigma)$ between two plates of surface area S separated by distance L, integration over the two patch particle spheres with radius R_p and R_p' in the Derjaguin approximation is performed to yield the force between two spheres at distance D, the shortest surface–surface distance between the particles,

$$F_C(D) = \int_0^{\phi_M} d\phi \frac{dS(\phi)}{L(\phi)^3}\vartheta_\parallel^{(d=3)}(L(\phi)/\xi_t, \Sigma), \tag{A3}$$

where the integral is over the angle ϕ, $dS(\phi)$ is the surface of an infinitesimal ring of radius $R\sin\phi$, and $L(\phi)$ is the distance between two such rings on the two spheres.

The isotropic V_C^{theory} then follows by integrating over the force. Realizing that only small ϕ contribute, a change of variables, rearrangement, and execution of (one of) the integrals gives[17,28,43,44]

$$\begin{aligned} V_C^{\mathrm{theory}}(D, R_p, R_p', \mathcal{Y}, \Sigma) &= \int_D^\infty dz F_C(z) \\ &= \frac{1}{D}\frac{2\pi R_p R_p'}{(R_p + R_p')}\int_1^\infty dx(x^{-2} - x^{-3})\vartheta_\parallel^{(d=3)}(x\mathcal{Y}, \Sigma) \\ &\equiv \frac{1}{D}\frac{2R_p R_p'}{(R_p + R_p')}\hat{\Theta}^{(d=3,\mathrm{Derj})}(\mathcal{Y}, \Sigma), \end{aligned} \tag{A4}$$

where in the last line we defined the function $\hat{\Theta}^{(d=3,\mathrm{Derj})}(\mathcal{Y}, \Sigma) \equiv \pi\int_1^\infty dx(x^{-2} - x^{-3})\vartheta_\parallel^{(d=3)}(x\mathcal{Y}, \Sigma)$. Note that in the Derjaguin approximation, the (critical Casimir) interaction strength is easily scaled according to the radii of the particles.

As $\vartheta_\parallel^{(d)}(\mathcal{Y}, \Lambda) = \vartheta_\parallel^{(d)}(\mathcal{Y}, \Sigma)$,[20] we can replace $\hat{\Theta}^{(d=3,\mathrm{Derj})}(\mathcal{Y}, \Sigma)$ with $\hat{\Theta}^{(d=3,\mathrm{Derj})}(\mathcal{Y}, \Lambda)$. For two spheres with equal radius, including the effect of the surface fields $w(h_s)$, we then finally arrive at

$$V_C^{\mathrm{theory}}(r) = \frac{R_p w^3}{D}\hat{\Theta}^{(d=3,\mathrm{Derj})}(\mathcal{Y}/w, \Lambda), \tag{A5}$$

where $r = D + 2R_p$ is the center-to-center distance, and we suppressed the functional dependence of $R_p, \mathcal{Y}, \Lambda$ and h_s. This is Eq. (4) arising in the main text.

APPENDIX B: POTENTIAL OPTIMIZATION

In this section, we detail how we construct the fit the potential. First, V_C is fitted as function of A and B to the numerical data, and A and B are again fitted to w and dT. Second, the construction of $V_{gravity}(z_i)$ is discussed. Third, the integration of the switching function S is explained.

1. Fit parameters for V_C

The critical Casimir attraction V_C^{theory} is fitted to Eq. (16) for $D \in [0.004, 0.025]\sigma$ with the curve_fit function of the scipy package in Python, which is a non-linear least-square fitting procedure. The fitting is performed for $w \in [0.40, 0.56]$, surface charge density $\Upsilon \in [-0.05, -0.38]e/\mathrm{nm}^2$, and $dT \in [0.12, 0.22]$ K. The values for A and B are again fitted to the functions,

$$A(w, dT) = \left(\sum_{x=0}^{3} a_x w^x\right)\left(\sum_{y=0}^{4} b_y dT^y\right), \tag{B1}$$

$$B(w, dT) = \left(\sum_{x=0}^{3} a_x w^x\right)\left(\sum_{y=0}^{4} b_y dT^y\right). \tag{B2}$$

Table V shows the resulting coefficients a and b.

TABLE V. Coefficients a and b valid for $w \in [0.40, 0.56]$, surface charge density $\Upsilon \in [-0.05, -0.38]e/\mathrm{nm}^2$, and $dT \in [012, 0.22]$ K for the calculation of A and B, as defined in Eqs. (B1) and (B2), respectively.

	A ($\sigma k_B T$)	B (σ)
a_0	−0.015 061 8	0.219 318 4
a_1	2.179 971 1	−6.415 286 9
a_2	−9.919 260 0	0.684 059 0
a_3	51.479 504 7	0.685 914 9
b_0	−0.226 173 2	−0.007 218 9
b_1	7.246 060 9	0.071 211 4
b_2	−60.600 308 3	−0.501 629 1
b_3	221.602 339 1	1.870 137 1
b_4	−304.832 948 0	−2.783 413 5

2. Gravity

As experimentalists on Earth see their patchy particles at the bottom of the sample due to the gravitational force pulling the colloids down, we add gravity to the model. The gravitational energy is defined as

$$V_g(z) = mgz = -F_g z, \tag{B3}$$

where m is the mass, g is the gravitational acceleration (on Earth in this case), z is the height, and F_g is the gravitational force. In order to know the effective gravitational force acting on the colloids, we need the mass difference between the colloid and the solvent,

$$\Delta m = \frac{4}{3}\pi r_{\text{colloid}}^3(\phi_{\text{TPM}}\rho_{\text{TPM}} + \phi_{\text{PS}}\rho_{\text{PS}} - \rho_{\text{sol}}), \tag{B4}$$

where r_{colloid} is the radius of the colloid, ϕ_x is the fractional volume, and ρ_x is the density of material x and the water–lutidine solution.

For the synthesis of dipatch particles,[1] three spheres of polystyrene (PS) surrounding one sphere of 3-(trimethoxysilyl)propyl methacrylate (TPM). The fractional volumes are estimated by assuming that the spheres are touching such that the ratio of the radii is $r_{\text{TPM}} : r_{\text{PS}} = -1 + 2/\sqrt{3}$. We calculate a volume fraction $\phi_{\text{TPM}} = 0.0012$.

While the patch material is clearly distributed anisotropically, we do not expect a gravitational torque acting on the patchy particles. Only a very small fraction TPM is used in the synthesis, which means that the patchy particle does not deviate much from an isotropic sphere.

For a dipatch particle with radius $r = 0.5\sigma$, the following values are used:

$$\begin{aligned}
&\phi_{\text{TPM}} = 0.0012,\\
&\phi_{\text{PS}} = 1 - \phi_{\text{TPM}},\\
&\rho_{\text{TPM}} = 1.235\ \text{g/ml},^{45}\\
&\rho_{\text{PS}} = 1.05\ \text{g/ml},^{46}\\
&\rho_{\text{sol}} = 0.989\ 66\ \text{g/ml},^{47}\\
&g = 9.806\ 65\ \text{m/s}^2.
\end{aligned}$$

This results in $F_g = -7.7\ k_{\text{B}}\text{T}/\sigma$ for the dipatch particles corresponding to a gravitational height of 0.13σ. Solving the equations in Eq. (14) with $\epsilon_{\text{LJ}} = 500 k_{\text{B}}T$ gives values for $b = 8.64\ k_{\text{B}}T$ and $z_{\text{cut}} = 1.12\sigma$.

3. Calculation of the switching function

We calculate the switching function from a direct evaluation of the patch–patch Casimir attraction V_{pp} by performing a (numerical) integration over the two surfaces of the patches in various configurations in which the particles are placed at the minimum energy position r_{min}, with specific patch angles θ_i, θ_j, and θ'_{ij},

$$V_{pp}(r_{\text{min}}, \theta_i, \theta_j, \theta'_{ij}) = \int_{D=0}^{D=\infty} V_{area}(D)dA, \tag{B5}$$

where $D = r - 2R$ is the surface–surface distance, V_{area} is the local Casimir potential energy per area, and dA is a small subarea on the patch surface.[44] We can approximate this effective interaction by performing a summation over N_A small subareas dA on both patch surfaces,

$$\begin{aligned}
V_{pp}(r_{\text{min}}, \theta_i, \theta_j, \theta'_{ij}) &\approx \sum^{N_A} V_{\text{area}}(D)\\
&\approx \alpha\frac{1}{2}\sum_{x=i,j}^{N_A^x} V_{\text{C}}(D^x_{\text{min}}),
\end{aligned} \tag{B6}$$

where we compute $V_{\text{area}}(D)$ from the critical Casimir interaction $V_C(r)$ for each of these N_A subareas on particle $x = i, j$ using the closest distance D^x_{min} to the patch surface on the other particle, as schematically illustrated in Fig. 12. As V_{area} has units of energy per area, whereas V_C is in units of energy, we insert an arbitrary prefactor α to make this conversion. We do not calculate this correction factor α explicitly. Instead, for the calculation of the integrated switching function S^{int} in Eq. (B7), we normalize the integration to the conformation where the patches are perfectly aligned, i.e., $\theta_i = \theta_j = \theta'_{ij} = 0°$,

$$\begin{aligned}
S^{int}(\theta_i, \theta_j, \theta'_{ij}) &= \frac{V_{pp}(r_{\text{min}}, \theta_i, \theta_j, \theta'_{ij})}{V_{pp}(r_{\text{min}}, \theta_i = \theta_j = \theta'_{ij} = 0°)}\\
&= \frac{\sum_{x=i,j}^{N_A^x} V_{\text{C}}(D^x_{\text{min}}; \theta_i, \theta_j, \theta'_{ij})}{\sum_{x=i,j}^{N_A^x} V_{\text{C}}(D^x_{\text{min}}; \theta_i = \theta_j = \theta'_{ij} = 0°)}.
\end{aligned} \tag{B7}$$

The N_{A} small equal areas of the summation are generated using an icosphere. An icosphere is a spherical shape composed of equally sized triangles, and by definition, the triangles' corners are uniformly distributed along the surface of the sphere. Thus, summing over these triangles' corners mimics the summation over N_{A}. In addition, to simplify the integration, we assume the curvature of the patch is equal to the curvature of the colloidal bulk particle.

The top row of Fig. 13 shows S^{int} of Eq. (B7) for the potential with $w = 0.462$, $\Upsilon = -0.090\ e/\text{nm}^2$, and $\theta_p = 19.5°$ at $dT = 0.16$ K. For this integration, we used $N_A \sim 4730$ for each particle. The three plots

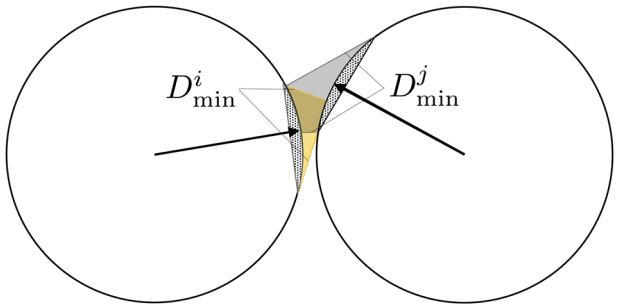

FIG. 12. The patch–patch interaction is calculated by integrating over both patch surfaces. The yellow and dark-colored areas for the particle on the left and right schematically indicate the volumes in which the N_A distances D^x_{min} lie, respectively.

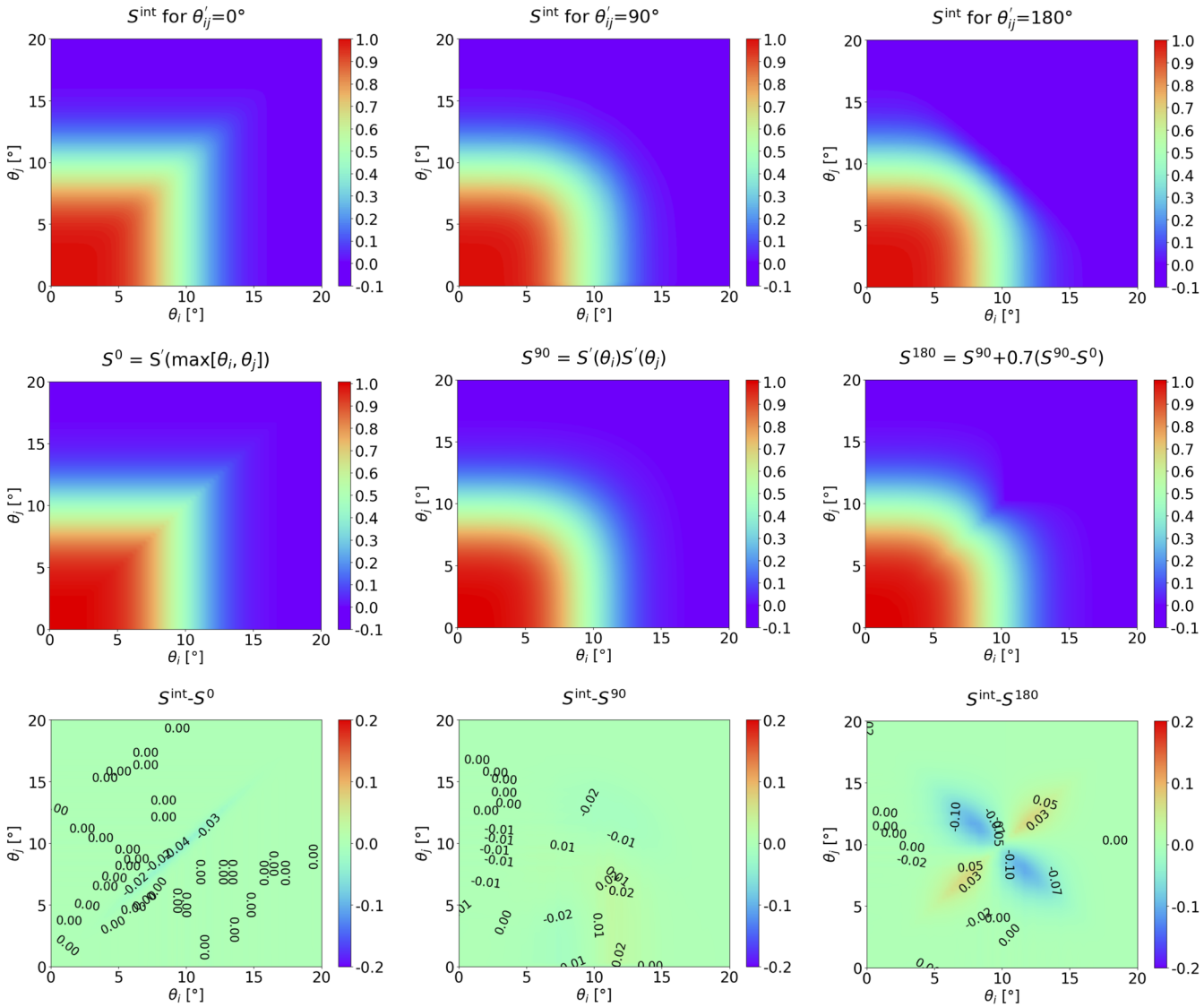

FIG. 13. S^{int} (top row); estimated switch functions S^0, S^{90}, and S^{180} (middle row) [Eqs. (B9)–(B11), respectively]; and difference between S^{int} and S^0, S^{90}, and S^{180} (bottom row) for θ'_{ij} = 0°, 90°, and 180° using an isotropic potential with w = 0.462, Υ = −0.090 e/nm^2, θ_p^{eff} = 19.5°, and dT = 0.16 K.

show how the interaction energy changes upon rotating the colloidal particles with angles θ_i and θ_j while $\theta'_{ij} = 0°$, 90°, or 180°.

Next, we would like to construct an approximation of S^{int} based on knowing only the switch function at $S^{int}(\theta_i, \theta_j = 0°)$. This part of the switching function S is fitted with the function

$$S'(\theta) = \exp\left(\sum_{l=2}^{8} c_l \theta^l\right) \tag{B8}$$

by using the curve_fit function of SciPy. The sum runs from 2 to ensure that the first derivative of S′ is zero at $\theta = 0°$. It runs up to 8, as the fitting procedure was not able to include more terms to improve the fit. In Table VI, the coefficients for the switching function of the benchmarked potential with w = 0.462, Υ = −0.090 e/nm^2, θ_p^{eff} = 19.5° and $dT \in [012, 0.22]$ K are shown.

From S', we construct the functions S^0, S^{90}, and S^{180} defined, respectively, as

$$S^0(\theta_i, \theta_j) = S'(\max(\theta_i, \theta_j)), \tag{B9}$$

$$S^{90}(\theta_i, \theta_j) = S'(\theta_i)S'(\theta_j), \tag{B10}$$

$$S^{180}(\theta_i, \theta_j) = S^{90}(\theta_i, \theta_j) + 0.7(S^{90}(\theta_i, \theta_j) - S^0(\theta_i, \theta_j)). \tag{B11}$$

TABLE VI. Coefficients c of S' in Eq. (B8) for which θ has units of degrees and $w = 0.462$, $\Upsilon = -0.090$ e/nm^2, $\theta_p^{\text{eff}} = 19.5°$, and $dT \in [012, 0.22]$ K.

dT	0.12	0.14	0.16	0.18	0.20	0.22
c_2	$-9.904\,139\,9 \times 10^{-4}$	$-8.620\,336\,2 \times 10^{-4}$	$-6.932\,609\,8 \times 10^{-4}$	$-4.558\,825\,7 \times 10^{-4}$	$-1.671\,990\,5 \times 10^{-4}$	$1.184\,130\,9 \times 10^{-4}$
c_3	$4.828\,195\,4 \times 10^{-4}$	$5.508\,159\,5 \times 10^{-4}$	$4.618\,313\,5 \times 10^{-4}$	$2.308\,458\,7 \times 10^{-4}$	$-8.348\,993\,0 \times 10^{-5}$	$-3.982\,680\,9 \times 10^{-4}$
c_4	$-2.685\,575\,6 \times 10^{-4}$	$-2.365\,735\,8 \times 10^{-4}$	$-1.482\,462\,4 \times 10^{-4}$	$-1.664\,963\,2 \times 10^{-5}$	$1.319\,285\,6 \times 10^{-4}$	$2.663\,086\,1 \times 10^{-4}$
c_5	$2.701\,451\,3 \times 10^{-5}$	$1.650\,837\,2 \times 10^{-5}$	$-2.450\,417\,4 \times 10^{-6}$	$-2.709\,200\,6 \times 10^{-5}$	$-5.273\,031\,4 \times 10^{-5}$	$-7.431\,187\,1 \times 10^{-5}$
c_6	$-1.766\,769\,6 \times 10^{-6}$	$-7.460\,324\,6 \times 10^{-7}$	$9.249\,552\,8 \times 10^{-7}$	$2.984\,924\,0 \times 10^{-6}$	$5.022\,323\,1 \times 10^{-6}$	$6.620\,356\,9 \times 10^{-6}$
c_7	$7.053\,160\,2 \times 10^{-8}$	$2.614\,785\,9 \times 10^{-8}$	$-4.391\,024\,3 \times 10^{-8}$	$-1.278\,794\,7 \times 10^{-7}$	$-2.077\,310\,3 \times 10^{-7}$	$-2.658\,646\,5 \times 10^{-7}$
c_8	$-1.351\,593\,4 \times 10^{-9}$	$-6.272\,305\,2 \times 10^{-10}$	$5.099\,754\,8 \times 10^{-10}$	$1.855\,298\,9 \times 10^{-9}$	$3.094\,941\,0 \times 10^{-9}$	$3.927\,019\,6 \times 10^{-9}$

Figure 13 shows these functions in the middle row and their difference with S^{int} in the bottom row. The functions were made by carefully inspecting the shape of the numerical results for S^{int} at 0°, 90°, and 180°. S^{int} at 0° and 90° are well approximated by S^0 and S^{90}, as one can see in the bottom row of Fig. 13. Inspecting S^{int} at 180° and $\max(\theta_i, \theta_j) < 5°$, one observes that it is almost identical to S^{90}. Only at $5° < \theta_i, \theta_j < 15°$, the value of S^{int} for 180° is lower than for 90°. In exactly this region, S^0 and S^{90} also show a difference. Therefore, S^{180} is constructed by adding to S^{90} the difference between S^0 and S^{90}.

To compose a functional solution for S as a function of θ_i, θ_j, and θ'_{ij} as a linear combination of S^0, S^{90}, and S^{180},

$$S^{lin.\ comb.} = \begin{cases} S^0(\lambda - 1) + S^{90}\lambda, & \lambda = \theta'_{ij}/90° \le 1, \\ S^{90}(2 - \lambda) + S^{180}(\lambda - 1), & \lambda > 1, \end{cases} \tag{B12}$$

where $\lambda = \theta'_{ij}/90°$. The discrepancy between $|S^{\text{int}} - S^{\text{lin. comb.}}| \le 10\%$ and lies mainly in a region where S^{int} is ~0.5, which means it is not a highly occupied region. The coefficient 0.7 in S^{180} was chosen to minimize the discrepancy between $S^{\text{lin. comb.}}$ and S^{int} for $90° < \theta'_{ij} < 180°$.

We simulate the chain length distribution and persistence length to test the sensitivity of the choice of switch function S. Figure 14 shows the persistence length of a 15-particle long chain and the chain length distribution of 1000 dipatch particles with gravity at the three test cases in which the switching function S is S^0, S^{90}, or $S^{\text{lin. comb.}}$. The persistence length of S^0 and $S^{\text{lin. comb.}}$ is similar, which seems to indicate that the chains under gravity have θ'_{ij} around 0°. However, the switching function S^{90} shows a stronger temperature dependence on the persistence length.

While the choice of switching function is substantially influencing the persistence length, it turns to have only a minor effect on the chain length distribution, as seen in Fig. 14. Advantages of S^{90} are its simple form and its dependence on the orientation of both particles. As S^0 leads to discontinuous torques due to the max function, another advantage of S^{90} is its continuous torques in a molecular dynamics simulation. Therefore, the switching function S used in Eq. (8) has the form of S^{90}.

4. Parameter list

For completeness, we compose a list with all the parameters and functions used in the model in Table VII.

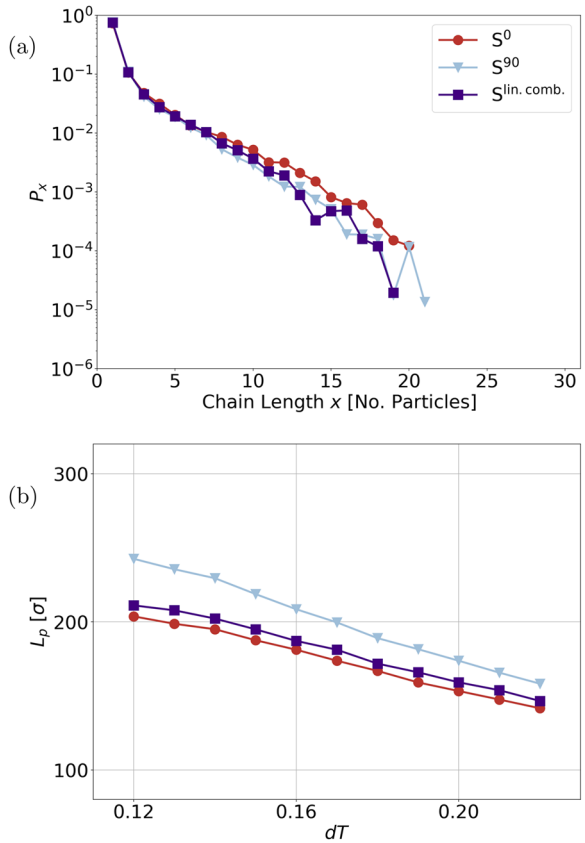

FIG. 14. Chain length distribution P_x (a) and persistence length L_p (b) of using function S as S^0, S^{90}, or $S^{\text{lin. comb.}}$ with $w = 0.462$, $\Upsilon = -0.090$ e/nm^2, $\theta_p^{\text{eff}} = 19.5°$, and $dT = 0.16$ K.

TABLE VII. Grouped by topic (indicated in boldface), this table lists all the functions and parameters including their symbol, description, value, unit, and reference. The given values are for the benchmarked dipatch particle potential.

Symbol	Description	Value	Unit	References
T	Temperature		K	
β	Inverse temperature		$1/k_\mathrm{B}\mathrm{T}$	
	Potentials			
$V_\mathrm{isotropic}$	Isotropic potential of a spherical colloidal particle [Eq. (1)]		$k_\mathrm{B}\mathrm{T}$	21
V_Yukawa	Isotropic repulsive electrostatic Yukawa potential		$k_\mathrm{B}\mathrm{T}$	
$V_\mathrm{C}^\mathrm{theory}$	Theoretical critical Casimir interaction (acquired as numerical data)		$k_\mathrm{B}\mathrm{T}$	21
V_C	Analytical interpolation of $V_\mathrm{C}^\mathrm{theory}$		$k_\mathrm{B}\mathrm{T}$	
V_pair	Patchy particle pair potential		$k_\mathrm{B}\mathrm{T}$	
$V_{\mathbf{p}_{ik},\mathbf{p}_{jl}}$	Patch–patch potential		$k_\mathrm{B}\mathrm{T}$	
S'	The fitted switching function			
$S_{\mathbf{p}_{ik},\mathbf{p}_{jl}}$	The switching function of the effective patch–patch interaction of $\mathbf{p}_{ik}$ and $\mathbf{p}_{jl}$			
V_gravity	The external field caused by the gravity and cell boundary		$k_\mathrm{B}\mathrm{T}$	
dT	$T_{cx} - T$		K	
	Gravitational parameters			
ϵ_LJ	A self-chosen value: It represents the steep potential of the capillary wall	500	$k_\mathrm{B}\mathrm{T}$	
Δm	The mass difference between the solvent and the particle	1.04	pg	
z_height	Gravitational height	0.13	σ	
	Solvent properties			
κ^{-1}	Debye length of the binary lutidine/water (25/75vol. %) mixture including 1 mM $MgSO_4$	2.78	nm	
λ_B	Bjerrum length	2.14	nm	
c	Composition of the binary liquid	25	Vol. % lutidine	
c_c	Critical luditine mass fraction of the water and lutidine binary mixture	0.287		38
$\mathcal{B}$	Non-universal scaling constant of the water lutidine solution without salt	0.765	fc_c^{-1}	39
c_salt	Salt concentration, $MgSO_4$	0.375	mM	
T_c	Critical temperature of the binary lutidine/water mixture	33.68	°C	38 and 48
T_{cx}	Phase separation temperature	$T_c + 0.08$	K	
$\xi_{t,+}^{(0)}$	The solvent correlation length of the binary liquid related to t	0.198	nm	21
	Scaling functions and parameters			
$\hat{\Theta}$	A universal scaling function			
t	Scaled temperature $(T_c - T)/T_c$			
h_b	Bulk ordering field			
μ	Chemical potential			
ξ	Solvent correlation length			
$\mathcal{Y}$	Scaling function related to the scaled temperature t			
Λ	Scaling function related to the bulk ordering field h_b			
ν	Universal scaling exponent	0.63		34
β	Universal scaling exponent used in the relation $\frac{T_{cx}-T_c}{T_c} = \left(\frac{c_c-c}{\mathcal{B}}\right)^{1/\beta}$	0.3265		34
δ	Universal scaling exponent	4.798		34
h_s	Surface field, describes the surface preference of the binary liquid			
w	Scaling wetting parameter, a function of surface field h_s	0.462		29 and 33

TABLE VII. *(Continued.)*

Symbol	Description	Value	Unit	References
	Particle properties and physical dimensions			
Z	Charge of the particle		e	
Υ	Surface charge density	−0.090	e/nm^2	
d_p	Projected patch diameter (AFM)	0.58(5)	μm	2 and 22
θ_p	Patch diameter (AFM)	21(2)	°	2 and 22
R_p	Patch particle radius of curvature (AFM)	1.0(2)	μm	2 and 22
σ	Diameter of bulk particle (AFM)	3.2(1)	μm	2 and 22
h_p	Height of the patch (AFM)	0.58(5)	μm	2 and 22
σ_c	Diameter of particle used in Yukawa potential, equals $2R_p$	2.0	μm	
n_p	Number of patches of the patchy particle	2		
θ_p^{eff}	The effective patch width used in the integration of S^{int}	19.5	°	
	Particle's positional and orientational variables			
$\mathbf{r}_{ij}$	The interparticle vector from particle i to j			
r	Center-to-center distance between two particles, $\lvert\mathbf{r}_{ij}\rvert$		σ	
D	Surface–surface distance between two spherical particles, $r-\sigma$		σ	
D_{min}	Surface–surface distance at which $V_{\text{isotropic}}(D_{\text{min}}) = \min(V_{\text{isotropic}})$	0.0068	σ	
$D_{\text{edge-edge}}$	Distance from the edge of the patch, to the edge of the other patch, when $\theta_i, \theta_j = 0°$, $2h_p + D_{\text{min}}$	0.035	σ	
$\mathbf{p}_{ik}$	kth patch vector of particle i			
θ_i, θ_j	Angle between patch vector and interparticle vector		°	
θ'_{ij}	Patch vectors' projected angle on the plane perpendicular to the interparticle vector		°	
Ω_i	(4D) quaternion representation of the orientation of particle i			
	Observables			
P_x	Probability of finding a chain of length x			
L_p	Persistence length		σ	
a_n	The amplitude of the nth bending mode in the worm-like-chain model [Eq. (17)]		σ	40 and 41
L	Contour length of the chain [Eq. (17)]		σ	40 and 41

DATA AVAILABILITY

The data that support the findings of this study are available within the article and its Appendix. The coefficients for the switching function S' [Eq. (9)] of potentials other than the benchmarked potential are available from the corresponding author upon reasonable request.

REFERENCES

[1] Z. Gong, T. Hueckel, G.-R. Yi, and S. Sacanna, Nature **550**, 234 (2017).
[2] S. G. Stuij, H. J. Jonas, Z. Gong, S. Sacanna, T. Kodger, P. G. Bolhuis, and P. Schall (2021) (unpublished).
[3] P. J. M. Swinkels, S. G. Stuij, Z. Gong, H. Jonas, N. Ruffino, B. V. D. Linden, P. G. Bolhuis, S. Sacanna, S. Woutersen, and P. Schall, Nat. Commun. **12**, 2810 (2021).
[4] Y. Wang, Y. Wang, D. R. Breed, V. N. Manoharan, L. Feng, A. D. Hollingsworth, M. Weck, and D. J. Pine, Nature **491**, 51 (2012).
[5] J. R. Wolters, G. Avvisati, F. Hagemans, T. Vissers, D. J. Kraft, M. Dijkstra, and W. K. Kegel, Soft Matter **11**, 1067 (2015).
[6] T. Nguyen, A. Newton, D. Kraft, P. Bolhuis, and P. Schall, Materials **10**, 1265 (2017).
[7] S. Stuij, J. M. van Doorn, T. Kodger, J. Sprakel, C. Coulais, and P. Schall, Phys. Rev. Res. **1**, 023033 (2019).
[8] F. Sciortino, E. Bianchi, J. F. Douglas, and P. Tartaglia, J. Chem. Phys. **126**, 194903 (2007).
[9] E. Bianchi, P. Tartaglia, E. La Nave, and F. Sciortino, J. Phys. Chem. B **111**, 11765 (2007).
[10] J. Russo, P. Tartaglia, and F. Sciortino, Soft Matter **6**, 4229 (2010).
[11] L. Rovigatti, D. de las Heras, J. M. Tavares, M. M. Telo da Gama, and F. Sciortino, J. Chem. Phys. **138**, 164904 (2013).
[12] K. T. Nguyen and C. De Michele, Eur. Phys. J. E **41**, 141 (2018).
[13] S. Roldán-Vargas, L. Rovigatti, and F. Sciortino, Soft Matter **13**, 514 (2017).
[14] A. C. Newton, R. Kools, D. W. H. Swenson, and P. G. Bolhuis, J. Chem. Phys. **147**, 155101 (2017).
[15] A. C. Newton, J. Groenewold, W. K. Kegel, and P. G. Bolhuis, Proc. Natl. Acad. Sci. U. S. A. **112**, 15308 (2015).
[16] A. C. Newton, T. A. Nguyen, S. J. Veen, D. J. Kraft, P. Schall, and P. G. Bolhuis, Soft Matter **13**, 4903 (2017).
[17] A. Gambassi, J. Phys.: Conf. Ser. **161**, 012037 (2009).
[18] F. Soyka, O. Zvyagolskaya, C. Hertlein, L. Helden, and C. Bechinger, Phys. Rev. Lett. **101**, 208301 (2008).

[19]N. Farahmand Bafi, P. Nowakowski, and S. Dietrich, J. Chem. Phys. **152**, 114902 (2020).
[20]T. F. Mohry, S. Kondrat, A. Maciołek, and S. Dietrich, Soft Matter **10**, 5510 (2014).
[21]S. G. Stuij, M. Labbé-Laurent, T. E. Kodger, A. Maciołek, and P. Schall, Soft Matter **13**, 5233 (2017).
[22]S. G. Stuij, J. Rouwhorst, H. J. Jonas, N. Ruffino, Z. Gong, S. Sacanna, P. G. Bolhuis, and P. Schall (2021) (unpublished).
[23]A. Maciołek and S. Dietrich, Rev. Mod. Phys. **90**, 045001 (2018).
[24]W. B. Russel, D. A. Saville, and W. R. Schowalter, *Colloidal Dispersions*, Cambridge Monographs on Mechanics (Cambridge University Press, 1989).
[25]J.-P. Hansen and H. Löwen, Annu. Rev. Phys. Chem. **51**, 209 (2000).
[26]V. A. Parsegian, *Van Der Waals Forces: A Handbook for Biologists, Chemists, Engineers, and Physicists* (Cambridge University Press, 2005).
[27]O. Vasilyev and A. Maciołek, J. Non-Cryst. Solids **407**, 376 (2015).
[28]A. Hanke, F. Schlesener, E. Eisenriegler, and S. Dietrich, Phys. Rev. Lett. **81**, 1885 (1998).
[29]O. A. Vasilyev and S. Dietrich, Europhys. Lett. **104**, 60002 (2013).
[30]M. Tröndle, O. Zvyagolskaya, A. Gambassi, D. Vogt, L. Harnau, C. Bechinger, and S. Dietrich, Mol. Phys. **109**, 1169 (2011).
[31]M. Fisher and P. de Gennes, C. R. Acad. Sci. Paris B **287**, 207 (1978).
[32]F. Pousaneh, A. Ciach, and A. Maciołek, Soft Matter **10**, 470 (2014).
[33]T. F. Mohry, A. Maciołek, and S. Dietrich, Phys. Rev. E: Stat., Nonlinear, Soft Matter Phys. **81**, 061117 (2010).
[34]A. Pelissetto and E. Vicari, Phys. Rep. **368**, 549 (2002).
[35]K. Sadakane, A. Onuki, K. Nishida, S. Koizumi, and H. Seto, Phys. Rev. Lett. **103**, 167803 (2009).
[36]K. Sadakane, M. Nagao, H. Endo, and H. Seto, J. Chem. Phys. **139**, 234905 (2013).
[37]F. Pousaneh and A. Ciach, Soft Matter **10**, 8188 (2014).
[38]A. Stein, S. J. Davidson, J. C. Allegra, and G. F. Allen, J. Chem. Phys. **56**, 6164 (1972).
[39]T. F. Mohry, A. Maciołek, and S. Dietrich, J. Chem. Phys. **136**, 224902 (2012).
[40]F. Gittes, B. Mickey, J. Nettleton, and J. Howard, J. Cell Biol. **120**, 923 (1993).
[41]C. P. Brangwynne, G. H. Koenderink, E. Barry, Z. Dogic, F. C. MacKintosh, and D. A. Weitz, Biophys. J. **93**, 346 (2007).
[42]M. Krech, Phys. Rev. E **56**, 1642 (1997).
[43]C. Hertlein, L. Helden, A. Gambassi, S. Dietrich, and C. Bechinger, Nature **451**, 172 (2008).
[44]L. R. White, J. Colloid Interface Sci. **95**, 286 (1983).
[45]C. van der Wel, R. K. Bhan, R. W. Verweij, H. C. Frijters, Z. Gong, A. D. Hollingsworth, S. Sacanna, and D. J. Kraft, Langmuir **33**, 8174 (2017).
[46]See https://www.sigmaaldrich.com/catalog/product/sigma/89904 for Sigma Aldrich, Micro particles based on polystyrene.
[47]Y. Jayalakshmi, J. S. Van Duijneveldt, and D. Beysens, J. Chem. Phys. **100**, 604 (1994).
[48]S. Z. Mirzaev, R. Behrends, T. Heimburg, J. Haller, and U. Kaatze, J. Chem. Phys. **124**, 144517 (2006).